energies

MDPI

Article

Large-Signal Nonlinear Average Model for a Voltage-Controlled Flyback Converter

David Eduardo Giraldo-Hernández [1], Mario Andrés Bolaños-Navarrete [1,*], Fabiola Angulo [1], Gustavo Osorio [1], Nicols Astaiza [2], Juan David Mina-Casaran [2] and Wilder Herrera [2]

[1] Departamento de Ingeniería Eléctrica, Electrónica y Computación, Percepción y Control Inteligente (PCI), Facultad de Ingeniería y Arquitectura, Universidad Nacional de Colombia—Sede Manizales, Manizales 170003, Colombia; dgiraldohe@unal.edu.co (D.E.G.-H.); fangulog@unal.edu.co (F.A.); gaosoriol@unal.edu.co (G.O.)

[2] Rynova Research Group, Rymel Ingeniería Eléctrica S.A.S., Copacabana 051040, Colombia; joveninvestigador2@rymel.com.co (N.A.); direccioninnovacion@rymel.com.co (J.D.M.-C.); wilderherrera@rymel.com.co (W.H.)

* Correspondence: mabolanosn@unal.edu.co

Abstract: Flyback converters are popular in various electronic applications due to their efficiency, galvanic isolation, and voltage stepping-up. However, their modeling and analysis present significant challenges. Traditional switched models offer high precision but require extensive computational resources, which is impractical for large-scale simulations. The alternative linear large-signal models are effective for studying stability near fixed operating points but fall short in capturing transient dynamics, limiting their use in the analysis and design of large or complex systems. This paper presents a novel nonlinear approach for representing a proportional–integral (PI) voltage-controlled flyback converter operating in continuous conduction mode (CCM) that accurately captures transients while reducing the computational burden. Numerical simulations in a study case confirm that the model effectively captures the converter dynamics under various conditions, achieving steady-state errors below 0.07% and accelerations up to 54×. These results facilitate efficient design iterations across a broad range of applications, including renewable energy systems, battery charging, and electric vehicles.

Keywords: power converter; flyback converter; voltage control; nonlinear average model; continuous conduction mode; power converter application

check for updates

Academic Editor: Adolfo Dannier

Received: 9 November 2024
Revised: 23 December 2024
Accepted: 9 January 2025
Published: 21 January 2025

Citation: Giraldo-Hernández, D.E.; Bolaños-Navarrete, M.A.; Angulo, F.; Osorio, G.; Astaiza, N.; Mina-Casaran, J.D.; Herrera, W. Large-Signal Nonlinear Average Model for a Voltage-Controlled Flyback Converter. *Energies* **2025**, *18*, 451. https://doi.org/10.3390/en18030451

Copyright: © 2025 by the authors. Licensee MDPI, Basel, Switzerland. This article is an open access article distributed under the terms and conditions of the Creative Commons Attribution (CC BY) license (https://creativecommons.org/licenses/by/4.0/).

1. Introduction

The flyback converter is a popular topology in power electronics due to its simple structure and low component count, making it both cost-effective and easy to implement. This topology employs two magnetically coupled inductors, ensuring galvanic isolation while maintaining simplicity in implementation across a wide range of controllers [1,2]. Its notable voltage boost capability [3] further enhances its applicability in renewable energy systems [4,5], battery and capacitor charging [6], electric vehicles [7], and various industrial applications [8]. Despite these advantages, flyback converters face challenges at higher power levels and voltages, where the stress on power semiconductors can reduce efficiency and power density, often necessitating the use of auxiliary circuits, such as snubbers, to manage voltage spikes and protect components [9–11]. Furthermore, the inherent non-smooth switching behavior of solid-state devices in flyback converters requires modeling through piecewise linear differential equations [12,13]. These equations demand advanced

simulation tools [14–16], which increase computational complexity and simulation time, especially for tasks like controller design and transient and stability analysis in converter-dominated power systems [13,17].

Averaged models allow for a simplified description of the dynamics of the system [18–21], although in some cases they do not accurately describe the entire operating range of the converter or require integration times in the range of microseconds [22]. In the literature, there are two dominant strategies for constructing averaged models. One involves capturing the converter's dynamics cycle by cycle using the transitions of the switches to build a discrete model. The alternative is to build continuous models, which, although more complex, capture the dynamic behavior over broader operating ranges and also allow larger integration times (i.e., in the range of milliseconds, typically) [13,19,20,23–26]. There are continuous linear and nonlinear averaged models. While linear models are widely used in the literature, largely due to their simplicity and usefulness for controller design and analysis around an operating point, they generally fail to capture the dynamic behavior of the transient. On the other hand, nonlinear models, although more complex to construct, allow for modeling the converter's dynamics over a wider range, including the transient. As a result, the range of applications of these models extends to larger and more complex systems that operate over slower time scales [24–26].

The literature presents several existing models, such as [27] that proposes a switching network linear average method. Ref. [28] uses a nonlinear model for predictive control on a flyback power factor correction rectifier. For the flyback converter, an equivalent averaged cell and state-space averaging is developed in [29]. An active clamp flyback based on state-space averaging is presented in [30]. Ref. [31] presents a bidirectional flyback inverter and uses state-space averaging; however, it does not capture the nonlinearities of the system. In [32], a novel nonlinear averaged model for a flyback converter operating under Peak Current Mode Control (PCMC) was proposed. The study included both numerical simulations and experimental validation, demonstrating high accuracy and significant reductions in computational time. However, the model derived in [32] was specific to PCMC, where the duty cycle dynamics were determined indirectly based on the charging dynamics of the capacitor, rather than directly from the instantaneous voltage values.

This paper addresses the limitations of event-driven and linear averaged models by proposing a nonlinear averaged model that bridges this gap, offering high accuracy in transient behavior modeling with reduced computational requirements. This advancement not only enhances the precision of power converter simulations but also facilitates their integration into broader system designs, where computational resources and real-time performance are critical. This is accomplished by deriving a mathematical expression that more accurately models the dynamics of the flyback converter. Consequently, a nonlinear model is obtained that effectively describes both transient and steady-state behavior with a low error margin. This model not only enhances accuracy but also offers computational efficiency, making it suitable for complex simulations where precision is essential. The proposed model is derived from a piecewise linear dynamic system, resulting in a nonlinear representation that is easy to simulate. This advancement not only enhances simulation accuracy but also facilitates the design of new controllers, expanding the model's applicability across a wide range of scenarios.

The rest of this paper is organized as follows. Section 2 describes the operation of the flyback converter with a proportional–integral (PI) voltage control loop. Next, in Section 3, the method for deriving the nonlinear averaged model from the state equations and certain assumptions is explained. Section 4 evaluates the model's performance under various conditions through numerical simulations, demonstrating both accuracy and efficiency. Moreover, a case study involving a photovoltaic cell with Maximum Power Point Tracking

(MPPT) is investigated to further evaluate and illustrate the potential of the proposed method in applications. Finally, Section 5 presents the conclusions and discusses the findings encountered during the development of this work. This last section includes some possible scenarios for future research.

2. Controlled Flyback Converter

The flyback converter shown in Figure 1 operates by using a transformer (i.e., coupled inductors) to store energy in its magnetic field during the ON phase of the cycle, and then transferring this energy to the load during the OFF phase. In this topology, the energy transfer is regulated by controlling the duty cycle of the switching device connected to the primary winding. A proportional–integral (PI) voltage controller adjusts the output based on the error between the reference voltage and the actual output voltage. This error is then fed into a pulse-width modulator (PWM) to set the peak current for each cycle. In the following section, we present a nonsmooth model for the controlled flyback converter.

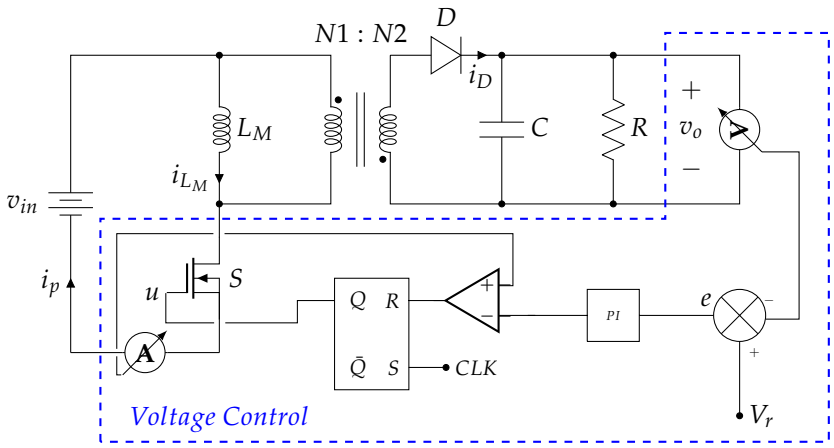


Figure 1. General schematic of a flyback converter with PI voltage control.

2.1. Flyback Converter Model

An ideal model of a PI-controlled flyback converter is shown in Figure 1. It consists of two coupled inductors with an associated magnetizing inductance L_M, which allows for a reduction in the dynamic model, a MOSFET (S), a diode (D), an output capacitor (C), and a load (R). The differential equations that define the dynamics using the magnetizing inductance and including the integral of the error for control are obtained based on the switch position. Thus, if the MOSFET is closed, the system is in topology 1 (T-1), and the system dynamics is described by Equation (1a)–(1c):

$$\dot{v}_C = -\frac{v_C}{RC} \tag{1a}$$

$$\dot{i}_{L_M} = \frac{v_{in}}{L_M} \tag{1b}$$

$$\dot{z} = V_r - v_C \tag{1c}$$

where v_C is the voltage across the capacitor, i_{L_M} is the magnetizing current, and z is the integral of the error, with V_r being the reference voltage. Similarly, v_{in} represents the input power supply voltage, and C, L_M, and R correspond to the values of capacitance, magnetizing inductance, and resistance, respectively. In this topology, the magnetizing

inductance is charged. Once the MOSFET opens, the system switches to topology 2 (T-2), and the system dynamics is described by Equation (2a)–(2c):

$$\dot{v}_C = -\frac{v_C}{RC} + n\frac{i_{L_M}}{C} \tag{2a}$$

$$\dot{i}_{L_M} = -n\frac{v_C}{L_M} \tag{2b}$$

$$\dot{z} = V_r - v_C \tag{2c}$$

where $n = N_1/N_2$ is the coupling factor, and N_1 and N_2 are the turns of the primary and secondary windings, respectively. Since this work analyzes the continuous conduction mode (CCM), no additional topologies are presented, and all the dynamics are defined by the set of Equations (1) and (2).

2.2. Flyback Converter Control

The general objective of the proposed control is to ensure a constant output voltage, even in the presence of disturbances in the load and input, while keeping the current within certain limits. To achieve this, two control loops are used. The first is a voltage feedback loop where PI control is applied to the error signal. The output signal from this control is then compared with the current of the primary winding, forming the second control loop, which is a current loop. Once these signals are compared, the result is sent to a flip-flop, and together with the clock, it generates the switching signal for the MOSFET. The process resets every T seconds, closing the MOSFET again. Thus, the control strategy establishes that the MOSFET is closed at the beginning of each cycle and remains in this position until the switching condition is met, which occurs at a generic time given by $t = kT + t_1$, where T is the clock cycle period. Once the switching condition is reached, the MOSFET opens and remains in this position until the start of the next cycle. The ratio t_1/T is known as the duty cycle and is denoted by d.

The control law governing the system behavior is defined in Equation (3):

$$u = \begin{cases} 1 & \text{if } i_{L_M} \leq k_p\, e + k_i\, z \ \wedge \\ & \quad t \in [kT\ kT + \text{mod}(t_1, T)] \\ 0 & \text{Otherwise} \end{cases} \tag{3}$$

For the system to operate in (CCM), it is necessary that:

$$i_{L_M} > 0,\ \forall\ t\ >\ 0$$

Figure 2 shows a time diagram of the control signal u and currents in the controlled system. It can be stated that the primary current (i_p) in the topology T-1, as given by Equation (1b), is equal to the magnetizing current. Similarly, the current in the secondary winding (i_p) in the topology T-2 is equal to $n\, i_{L_M}$ (See Equation (2b)). These relationships between the currents of the primary and secondary windings and the magnetizing current simplify the mathematical model, allowing the converter to be modeled as a second-order system. Note that i_p operates when the control signal u is active, while i_s operates in a complementary fashion.

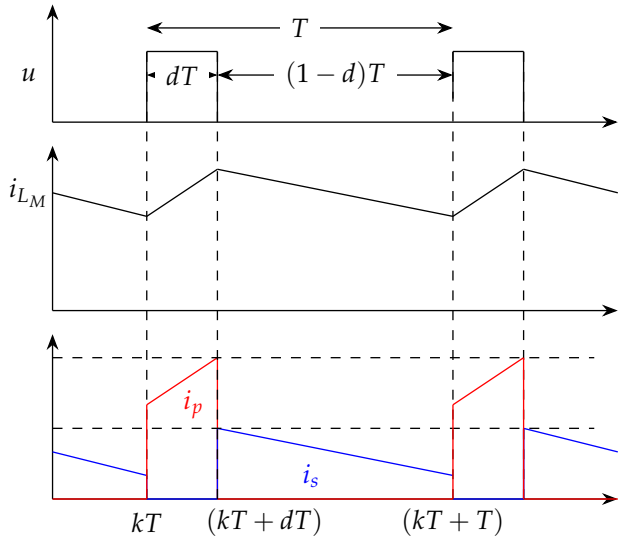


Figure 2. Flyback converter waveforms in CCM. The control signal u is shown at the top, followed by the magnetizing current i_{L_M} in the middle, and the primary i_p and secondary i_s winding currents at the bottom, all over one switching period.

3. Nonlinear Averaged Model (NAM) and PI Control Design

3.1. Proposed Model in Continuous Conduction Mode (CCM)

To develop an averaged model for the FC in CCM that includes the system's transient state, the following approach is taken. First, the magnetizing current $i_{L_{M-T2}}$ during T-2 is estimated as a function of the capacitor voltage v_C over one cycle. This is carried out by assuming a linear approximation between the current at $t = T + dT$, denoted by $i(dT)$, and the final current at $t = kT + T$, denoted by i_{end}. This common simplification strikes a balance between model accuracy and computational simplicity. The average value of the current delivered to the load and capacitor over a complete cycle, represented as $\bar{i}_{L_M}$, is then obtained by integrating $i_{L_{M-T2}}$ and dividing by the period T. This average current is used as an input for the state equation during the charging phase, as shown in (2a).

To more accurately estimate the existing waveform as illustrated in Figure 3, it can be noted that the overall current at T-2 (i.e., $\int_{T-2} i_{L_M}$) is depicted by the area under a trapezoid, leading to the linear approximation in Equation (4):

$$i_{L_{M-T2}} \approx (1-d)T\,\frac{i(dT) + i_{end}}{2}. \tag{4}$$

Assuming that v_C remains constant throughout the cycle simplifies calculations by directly approximating the current at the end of the cycle i_{end} with Equation (5) using (2b):

$$i_{end} \approx i(dT) - (1-d)T\,n\,\frac{v_C}{L_M}. \tag{5}$$

Inserting the expression for $(1-d)T$ obtained from (5) into (4) results in:

$$i_{L_{M-T2}} \approx L_M \frac{i^2(dT) - i_{end}^2}{2\,n\,v_C}. \tag{6}$$

To compute the average current $\bar{i}_{L_M}$ over one period, we divide Equation (6) by T. By substituting $\bar{i}_{L_M}$ into Equation (2a), we derive a differential equation for the capacitor voltage v_C in Equation (7):

$$\dot{v}_C = -\frac{v_C}{RC} + L_M \frac{i^2(dT) - i_{end}^2}{2\,T\,C\,v_C} \tag{7}$$

with $i(dT) = \frac{n\,v_C}{L_M}(1-d)\,T + i_{end}$. The key point of the analysis involves determining i_{end}, which represents the current at the end of the discharge period T-2 and serves as the initial current for the subsequent cycle. The approximation of i_{end} is carried out through the concatenation of Equations (8) and (9):

$$i(kT + dT) = i(kT) + \frac{v_{in}}{L_M} dT \;\forall\; t \in [kT, kT + dT] \tag{8}$$

$$i(kT + T) = i(dT) - n\frac{v_C}{L_M}(T - dT) \tag{9}$$

By calculating $i(kT + T) - i(kT)$ and dividing by T, the average dynamics of the desired current i_{end} is obtained and given by Equation (10):

$$\dot{i}_{end} = \frac{d(v_{in} + n\,v_C) - nv_C}{L_M} \tag{10}$$

Finally, to approximate the duty cycle, it is necessary to use the control law. Thus, considering the expression for the current in T-1 (i.e., Equation (1b)) and the control law in (3), the duty cycle is approximated by Equation (11):

$$d = \frac{L_M}{T\,v_{in}}(k_p\,V_r - k_p\,v_C + k_i\,z - i_{end}) \tag{11}$$

In this way, the averaged model is defined by the Equations (1c), (7), and (10), with the duty cycle given by (11).

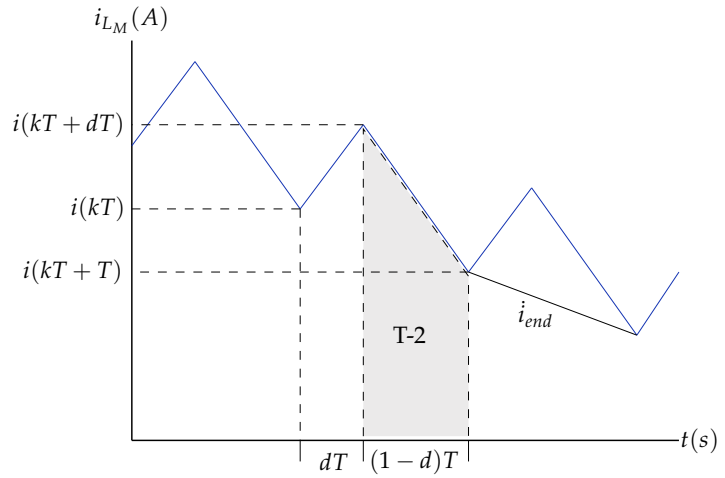


Figure 3. Transient i_{L_M} current waveform in CCM for the flyback converter. The figure presents the variation in i_{end} at the end of each cycle such as $i(kT + T)$ and $i(kT)$; the overall current at T-2 is calculated from the trapezoid area (in gray).

3.2. Control Design

This section describes the tuning process for the parameters k_p and k_i. Given that the proposed model is highly nonlinear and involves quadratic terms in the states as well as products between the control action and the states, the following tuning methodology is

proposed, consisting of an initial coarse tuning followed by fine adjustments to improve transient performance. From Equation (11), the control action is rewritten in Equation (12):

$$d(t) = \frac{L_M}{T\, v_{in}} \left(k_p \left(e(t) + 1/\tau_i \int e(t)dt \right) - i_{end} \right) \tag{12}$$

The proportional control action governs the transient behavior until the integral control takes over. Initially, k_p was tuned to ensure the duty cycle did not saturate during large changes. For a system starting close to rest and with a reference value of 100 V, the error in the output is large. Hence, k_p was set to 0.5 AV^{-1} to keep the duty cycle around half of its maximum value. In linear systems, the integral control typically takes over the plant in approximately $4\tau_i$. For a desired settling time of $t_s = 0.01$ s, τ_i was set to 0.0025 s, resulting in $k_i = 200$ $AV^{-1}s^{-1}$. After fine-tuning, the final values were adjusted to $k_p = 0.48$ AV^{-1} and $k_i = 200$ $AV^{-1}s^{-1}$. However, due to the inherent nonlinearities of the system, the actual settling time was shorter than expected.

4. Results and Application

The performance of the proposed nonlinear averaged model (NAM) will be assessed by comparing its behavior against the event-driven model (EM) and a standard averaged model (SAM) derived from [33,34] The response to changes in the reference will be examined, followed by an analysis under simultaneous changes in both the reference and the load. Finally, this section presents a study case for a photovoltaic system with maximum power point tracking (MPPT) using the nonlinear averaged model implemented in Matlab/Simulink® R2023b. The parameter values used in simulations are listed in Table 1. When changes are made, the new values will be specified.

Table 1. Simulation parameters.

Parameter	Values	Units
Input voltage (V_i)	12	V
Coupled inductors turns ratio ($n = N_1/N_2$)	1/30	
Magnetizing inductance (L_M)	9.85	µH
Period (T)	42.6	µs
Capacitor (C)	30	µF
Load resistance (R)	100	Ω
Reference voltage (V_r)	60	V
Proportional constant (k_p)	0.48	AV^{-1}
Integral constant (k_i)	200	$AV^{-1}s^{-1}$

4.1. Model Performance

Figure 4 shows simulations implemented in a MATLAB script. We perform the comparison between the event-driven model (EM) (yellow line) and the nonlinear averaged model (NAM) (blue dotted line). The errors between the two models (orange line) for voltage, current, and duty cycle are also depicted. For simplicity, the current for the EM is depicted only once per period (i.e., $t = kT$), which corresponds to the i_{end} values from the nonlinear averaged model. To obtain the average magnetizing current needed in Equation (7), we use $i(dT) = i_{end} + \frac{nv_C}{L_M}(1-d)\,T$. The initial conditions were $(v_C,\, i_{L_M},\, z) = (1.589,\, 28.517,\, 0)$ (Em), and $(v_C,\, i_{end},\, z) = (1.589,\, 28.517,\, 0)$ (NAM). A very good match is observed between the event-driven and the nonlinear averaged models. For voltage, the maximum error is 0.5%. For the current and duty cycle, the errors are even smaller. The maximum error in the current was less than 0.4%, while for the duty cycle, it was around 8%.

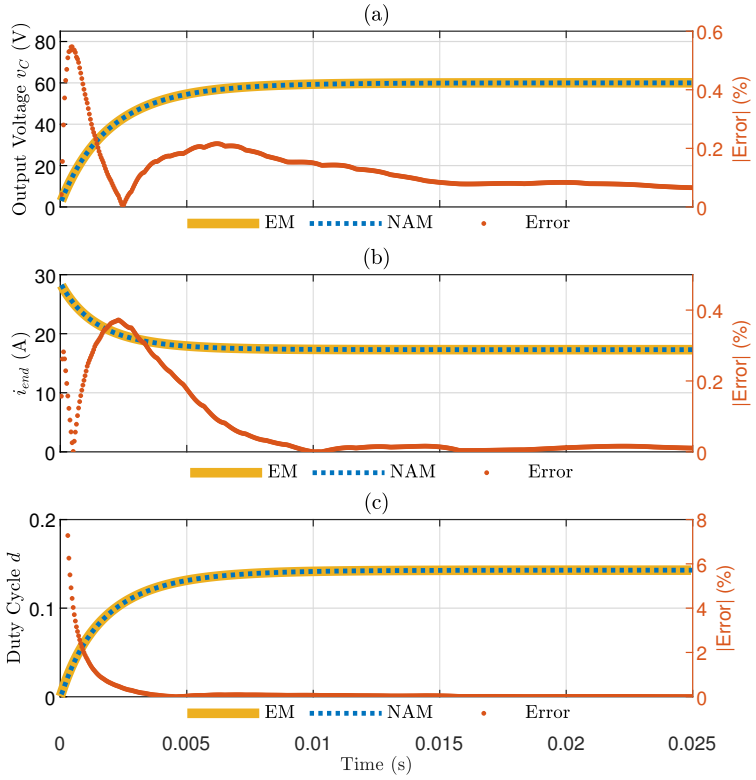


Figure 4. Absolute error of the nonlinear average model (NAM) for the controlled system. The event-driven model (EM) is the reference. The orange dotted line corresponds to the absolute error between the two models. (**a**) refers to the output voltage v_c. (**b**) corresponds to the current i_{end}. (**c**) indicates the duty cycle d.

Additionally, based on power converter theory [33,34], the expected steady-state value of the current at the beginning of the cycle is given by Equation (13):

$$i_{end} = \frac{v_C^2}{v_{in}\, d_{ss}\, R} - \frac{v_{in}\, d_{ss}\, T}{2\, L_M} \approx 17.2970 \text{ A} \tag{13}$$

and the duty cycle would be given by Equation (14):

$$d_{ss} = \frac{n\, v_C / v_{in}}{1 + n\, v_C / v_{in}} \approx 0.1428 \tag{14}$$

Thus, by analyzing the averaged model and calculating the steady-state values of Equations (10) and (11), the results are $i_{end} \approx 17.2970$ [A] and $d_{ss} \approx 0.1428$, showing complete agreement.

The performance of the system is also evaluated by analyzing the behavior of NAM in comparison to SAM. Figure 5 shows the reduced errors between these two methods for voltage, current, and duty cycle, indicating that both approaches effectively capture the dynamics of the system. The event-driven model was implemented by solving the differential Equations (1) and (2) using the ode15s solver in MATLAB, with event detection to accurately handle topology transitions during switching events. Conversely, the NAM was formulated based on (7), (10), and (11)and integrated using the ode15s solver without event detection, as the dynamics is continuous. Validation was performed by comparing the voltage, current, and duty cycle values of the NAM against those of the event-driven model (EM) and the standard averaged model (SAM) at each switching event.

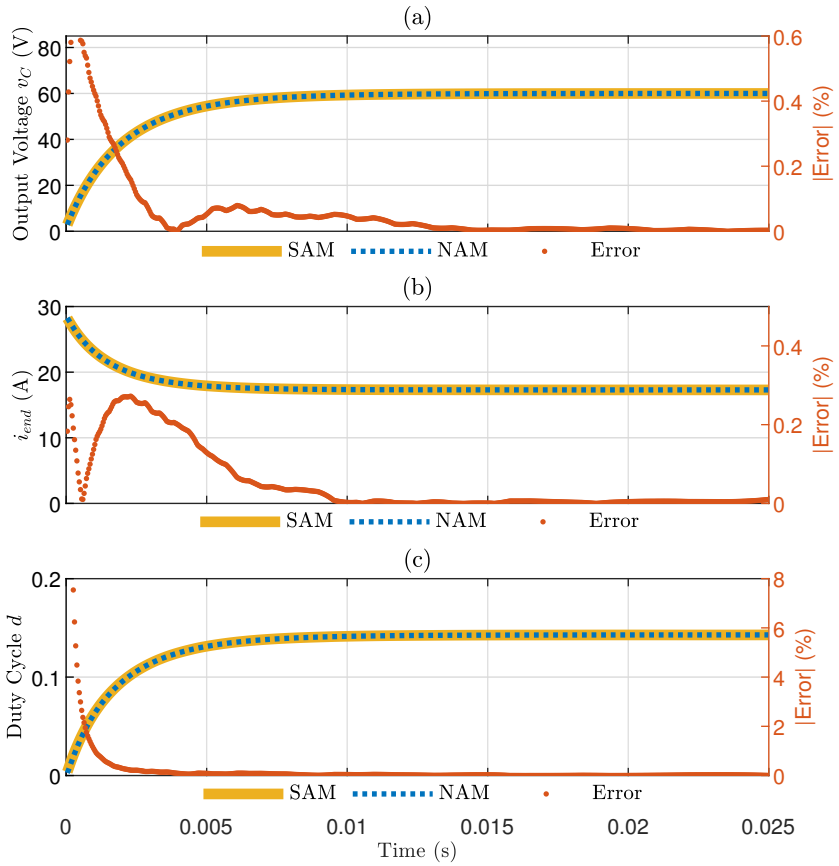


Figure 5. Comparison between SAM (yellow line) and NAM (blue dotted line). (**a**) corresponds to the output voltage v_c. (**b**) refers to the current i_{end}. (**c**) corresponds to the duty cycle d. The absolute error (orange dotted line) of the NAM model with respect to the SAM model is calculated for each signal.

4.2. Performance Under Disturbances

Figure 6 shows the behavior of both models (i.e., EM and NAM) under reference and load disturbances. The system starts from the initial conditions $(v_C, i_{L_M}, z) = (1.59, 28.52, 0)$ for EM and $(v_C, i_{end}, z) = (1.59, 28.52, 0)$ for NAM. From the initial condition, the system evolves to a reference voltage $V_r = 60$ V. At $t = 0.03$ s, the reference is changed to $V_r = 30$ V, then at $t = 0.06$ s it is changed to $V_r = 80$ V, and at $t = 0.09$ s the reference is simultaneously adjusted to $V_r = 40$ V and the load resistance to $R = 60\ \Omega$. When the system is perturbed, the transient presents a larger error that vanishes and the error in voltage, current, and duty cycle remains below 1%, even when the load and reference are varied simultaneously.

4.3. Averaged Nonlinear Application

Figure 7 illustrates the implementation of the averaged model applied in a solar energy generation system. In this configuration, the flyback converter (FC) is connected to a solar generator and an RC load. The **PV Source** block in the figure contains a 250 W solar panel, with irradiance and temperature values as inputs. To prevent abrupt changes in these parameters, a rate saturation block is included, ensuring that any fluctuations in irradiance or temperature are gradual and realistic.

At the output of the photovoltaic system, two stray capacitors are incorporated to emulate parasitic capacitance. Additionally, a coupling capacitor is placed between the PV array and the FC to match the dynamic characteristics of the PV panel with the input of the flyback converter. This coupling capacitor stabilizes the power flow, helping to prevent unwanted oscillations that may arise from the nonlinear behavior of the PV system.

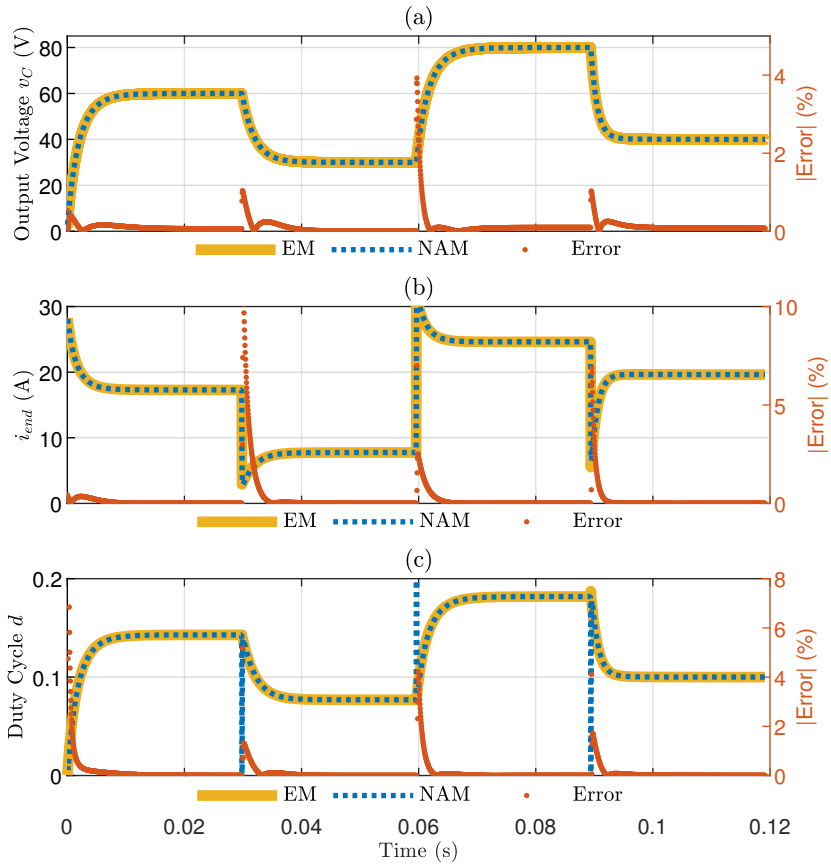


Figure 6. Response of the NAM and the event-driven model (EM) to disturbances. The orange dotted line indicates the error between variables. At $t = 0.03$ s, V_r changes from 60 V to 30 V; at $t = 0.06$ s V_r changes from 30 V to 80 V. Finally, at $t = 0.09$, V_r changes from 80 V to 40 V and R changes from 100 Ω to 60 Ω. (**a**) corresponds to the output voltage v_c. (**b**) refers to the current i_{end}. (**c**) corresponds to the duty cycle d.

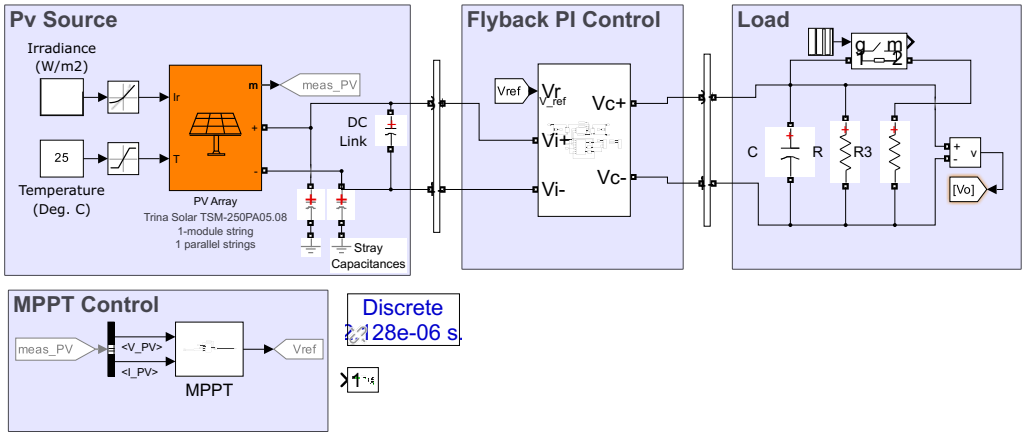


Figure 7. Application of the averaged model in a photovoltaic system for maximum power point tracking.

The **MPPT Control block** , located at the lower left of the figure, is responsible for extracting the maximum power from the PV array. It continuously monitors the voltage and current output of the PV panel to identify the maximum power point through a Perturb and Observe (P&O) algorithm. As environmental conditions fluctuate, the MPPT controller dynamically adjusts the voltage reference to ensure the system operates at this optimal power point, allowing for efficient energy extraction from the solar array.

In the **Flyback PI Control** block, the FC is controlled according to the voltage reference provided by the MPPT algorithm. This setup differs from previous applications, as here the control is applied at the input of the system, maintaining a constant input voltage as specified by the MPPT reference. The internal parameters of the model, including operating frequency, transformer turns ratio, and the inductance values in the primary and secondary windings, are consistent with previous applications. However, in this configuration, the PI controller gains are adjusted to $k_p = 50$ and $k_i = 100$ to achieve the desired performance in regulating the input voltage.

Following the FC, the **Load** block includes an RC circuit simulating a dynamic load condition. In this setup, the resistance changes over time by connecting an additional resistor in parallel, emulating a sudden load change. Although an RC load is used here, the system design is flexible and can support various load types. For instance, in grid-connected applications, a DC-AC inverter is typically connected at the output, allowing the generated energy to be injected into the electrical grid.

Figure 8 shows the results of applying the nonlinear averaged model integrated into a simulation in Simulink® R2023b, and its comparison with a switched model fully implemented in Simulink® R2023b, using SimPower elements.

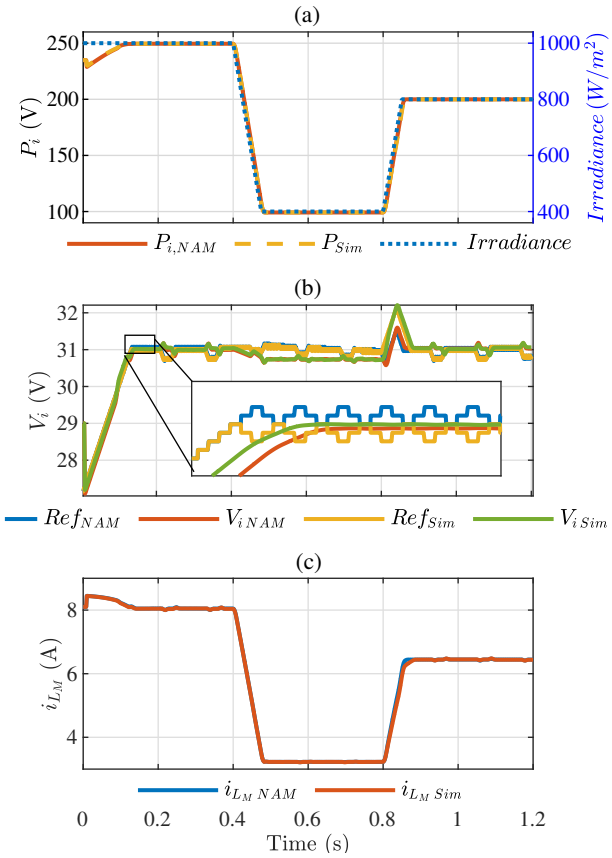


Figure 8. Comparison between the nonlinear averaged model (NAM) and the simulink switched model for the flyback converter. (**a**) Power extracted from the solar panel and irradiance levels, showing changes from 1000 W/m² to 400 W/m² at 0.4 s, and then to 800 W/m² at 0.8 s. (**b**) Reference voltage generated by the MPPT and input voltage to the flyback converter for both the NAM and switched model. (**c**) Current delivered by the photovoltaic generator for the NAM and switched model.

Figure 8a illustrates the power extracted from the panel (orange and yellow lines) and the irradiance to which the panel is exposed (blue dotted line), varying from 1000 W/m^2 to 400 W/m^2 in 0.4 s and then to 800 W/m^2 at 0.8 s. Initially, the extracted power is at

its maximum (250 W); after the first change in irradiance, the power decreases to 100 W, and following the second change, it increases to 800 W. This demonstrates that the MPPT algorithm, specifically the perturb and observe (P&O) method, functions correctly and ensures the extraction of maximum power.

Figure 8b presents the reference voltage generated by the MPPT and the input voltage to the FC for both the averaged model and the switched model. As observed, the reference signal in the nonlinear model (blue line) follows a discrete pattern due to the dynamics of the P&O method, while the input voltage (red line) exhibits continuous dynamics thanks to the filtering effect of the input capacitor. The reference voltage in the switched model (yellow line) and its input voltage (green line) also follow this continuous pattern.

Although the reference and input voltage signals initially exhibit similar behavior, the MPPT references show variations due to their high sensitivity to changes in irradiance conditions. This results in some differences in behavior between the averaged model and the switched model, particularly in response to abrupt changes in radiation.

In this last change in irradiance, the load resistance is also modified by activating the resistor $R_3 = 150\ \Omega$, which is in parallel with resistor R, resulting in an equivalent resistance of 60 Ω.

Figure 8c shows the current delivered by the photovoltaic generator. The blue and red lines are nearly superimposed, indicating that the averaged model very accurately reproduces the behavior of the switched model in Simulink® R2023b.

Figure 9 shows a close-up of the previous image in the interval from 0.75 s to 0.9 s. In this range, it can be observed that the reference signals of the averaged model and the switched model diverge during the irradiance change. This divergence is due to the behavior of the MPPT method, which responds differently in each model to radiation variation.

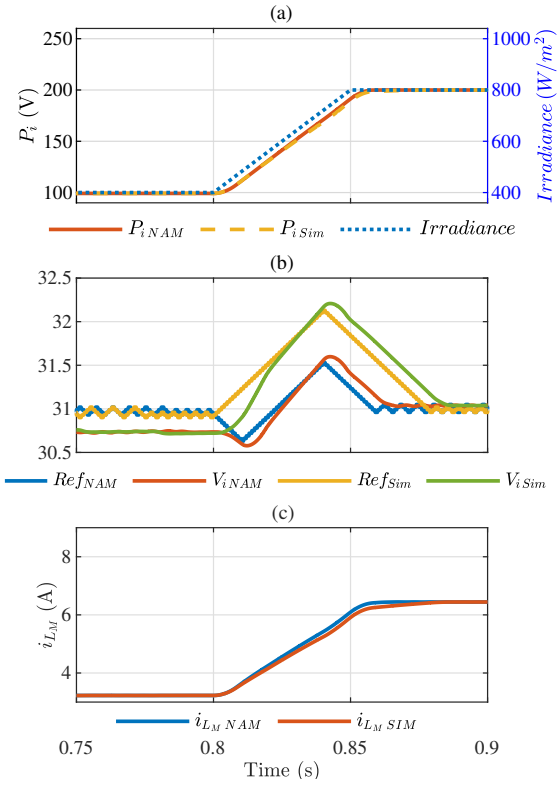


Figure 9. Differences due to the MPPT behavior between models. This zoomed figure highlights the discrepancies in response between the NAM and the simulink switched model for the FC during irradiance changes.(**a**) Power extracted from the solar panel and irradiance levels. (**b**) Reference voltage generated by the MPPT and input voltage to the flyback converter for both the NAM and switched model. (**c**) Current delivered by the photovoltaic generator for the NAM and switched model.

5. Conclusions and Future Work

This paper presents a novel nonlinear averaged model for a voltage-controlled flyback converter in CCM that accurately captures transients while reducing computational load and simulation time. In addition, the developed model enables the simulation of systems over much larger time scales with high precision.

This model can be integrated into different simulation environments, such as SPICE-based software or power systems stability analysis tools. These integrations would enable, for example, the study of the behavior of multiple photovoltaic generators connected to different nodes in an electrical network, optimizing their operation in distributed generation systems.

The developed model has proven to be effective across a broad operating range, as shown in Table 2, where the steady-state error is less than 0.07%, with an accuracy of 99.93%.

Table 2. Model response error.

		Transient Error [%]	Stable Error [%]
Without Disturbances	Voltage	<0.6	<0.2
	Current	<0.4	<0.02
	Duty cycle	<8	<0.005
With Disturbances	Voltage	<4	<0.08
	Current	<10	<0.007
	Duty cycle	<8	<0.004

Table 3 presents the simulation times obtained on a computer with a 7th generation Intel i7 processor (4.2 GHz) for two numerical implementations in Matlab/Simulink® R2023b (i.e., EM and NAM). As expected, the averaged nonlinear model required significantly less computation time compared to the high-resolution switched model, achieving an acceleration factor of 54×.

Table 3. Acceleration using the nonlinear averaged model (NAM).

Application	Simulink EM [s]	NAM [s]	Acceleration
MPPT	291.77	5.4	54×

The proposed model is valid under the assumption of CCM operation and relies on accurate linear approximations of current dynamics. Additionally, as the averaged model smooths the system dynamics, it is essential to verify the stability of the switched model before applying the averaged approach. Future work could explore extending the model to include the DCM operation, and also in studying the applicability of the proposed method to other converter topologies and control strategies. The modular structure of the proposed approach allows for straightforward adaptation to systems where the current dynamics can be approximated by linear polynomial equations.

Future research could also focus on integrating parasitic effects and internal resistances, as well as optimizing control parameters to further enhance the model's accuracy and efficiency.

Author Contributions: Validation, D.E.G.-H., M.A.B.-N. and G.O.; formal analysis, F.A.; investigation, D.E.G.-H. and M.A.B.-N.; writing—original draft preparation, D.E.G.-H., F.A. and M.A.B.-N.; writing—review and editing, D.E.G.-H., M.A.B.-N., F.A. and G.O.; supervision, F.A. and G.O.; project administration, N.A. and J.D.M.-C.; funding acquisition, W.H. All authors have read and agreed to the published version of the manuscript.

Funding: This work was supported by Universidad Nacional de Colombia, Rymel Ingeniería Eléctrica S.A.S., and Patrimonio Autónomo Fondo Nacional de Financiamiento para la Ciencia, la Tecnología y la Innovación Francisco José de Caldas—Ministerio de Ciencia, Tecnología e Innovación, under the project "Validación tecnológica para la fabricación de reconectadores automáticos para redes inteligentes, del tipo seco con polos encapsulados utilizando compuestos poliméricos termoestables", contract No. 099-2022.

Data Availability Statement: The original contributions presented in the study are included in the article; further inquiries can be directed to the corresponding author.

Acknowledgments: The authors would like to acknowledge the use of ChatGPT, an AI-based language model developed by OpenAI, for assisting with the translation of the manuscript from Spanish to English and for providing grammar and style corrections during the writing process.

Conflicts of Interest: Authors Nicols Astaiza, Juan David Mina-Casaran and Wilder Herrera were employed by the company Rymel Ingeniería Eléctrica S.A.S. The remaining authors declare that the research was conducted in the absence of any commercial or financial relationships that could be construed as a potential conflict of interest.

References

1. Gökçegöz, F.; Akboy, E.; Hülya Obdan, A. Analysis and design of a flyback converter for universal input and wide load ranges. *Electrica* **2021**, *21*, 235–241. [CrossRef]
2. Ramos-Paja, C.A.; Bastidas-Rodriguez, J.D.; Saavedra-Montes, A.J. Sliding-Mode Control of a Photovoltaic System Based on a Flyback Converter for Microinverter Applications. *Appl. Sci.* **2022**, *12*, 1399. [CrossRef]
3. Rashid, M.H. *Power Electronics: Devices, Circuits, and Applications*, 4th ed.; International Edition; Pearson: London, UK, 2014.
4. Pesce, C.; Riedemann, J.; Peña, R.; Degano, M.; Pereda, J.; Villalobos, R.; Maury, C.; Young, H.; Andrade, I. A modified multi-winding DC–DC flyback converter for photovoltaic applications. *Appl. Sci.* **2021**, *11*, 11999. [CrossRef]
5. Avila, A.; Garcia-Bediaga, A.; Alzuguren, I.; Vasic, M.; Rujas, A. A Modular Multifunction Power Converter Based on a Multiwinding Flyback Transformer for EV Application. *IEEE Trans. Transp. Electrif.* **2022**, *8*, 168–179. [CrossRef]
6. Calvo, C.R. Estudio de Paralelización de Convertidores Flyback en Aplicaciones de Carga de Baterías y Condensadores de Hasta 1.2 Kilovatios. Ph.D. Thesis, Universidad de León, León, Spain, 2023.
7. Vračar, D.Đ.; PEJOVIĆ, P.V. Active-Clamp Flyback Converter as Auxiliary Power-Supply of an 800 V Inductive-Charging System for Electric Vehicles. *IEEE Access* **2022**, *10*, 38254–38271. [CrossRef]
8. Vračar, D.; Pejović, P. Active-clamped flyback DC-DC converter in an 800V application: Design notes and control aspects. *J. Electr. Eng.* **2022**, *73*, 237–247. [CrossRef]
9. Sun, S.; Guo, H.; Zhang, Y.; Sun, L.; Li, Y.; Zhang, Y. Novel synchronous rectification strategy for flyback converter in both DCM and CCM applications. *IET Power Electron.* **2023**, *16*, 893–904. [CrossRef]
10. Zhu, B.; Yang, Y.; Wang, K.; Liu, J.; Vilathgamuwa, D.M. High Transformer Utilization Ratio and High Voltage Conversion Gain Flyback Converter for Photovoltaic Application. *IEEE Trans. Ind. Appl.* **2024**, *60*, 2840–2851. [CrossRef]
11. Tseng, S.Y.; Fan, J.H. Buck-Boost/Flyback Hybrid Converter for Solar Power System Applications. *Electronics* **2021**, *10*, 414. [CrossRef]
12. Ngo, K.D. Low frequency characterization of PWM converters. *IEEE Trans. Power Electron.* **1986**, *4*, 223–230. [CrossRef]
13. Shah, C.; Vasquez-Plaza, J.D.; Campo-Ossa, D.D.; Patarroyo-Montenegro, J.F.; Guruwacharya, N.; Bhujel, N.; Trevizan, R.D.; Rengifo, F.A.; Shirazi, M.; Tonkoski, R.; et al. Review of dynamic and transient modeling of power electronic converters for converter dominated power systems. *IEEE Access* **2021**, *9*, 82094–82117. [CrossRef]
14. Khader, S.; Hadad, A.; Abu-Aisheh, A.A. The application of PSIM & Matlab/Simulink in power electronics courses. In Proceedings of the 2011 IEEE Global Engineering Education Conference (EDUCON), Amman, Jordan, 4–6 April 2011; IEEE: Piscataway, NJ, USA, 2011; pp. 118–121.
15. Surya, S.; Chhetri, A.; Arjun, M.; Williamson, S. Effective power electronics understanding using circuit simulation. *IEEE Potentials* **2023**, *42*, 25–31. [CrossRef]
16. Estrada, L.; Vázquez, N.; Vaquero, J.; de Castro, Á.; Arau, J. Real-time hardware in the loop simulation methodology for power converters using labview FPGA. *Energies* **2020**, *13*, 373. [CrossRef]
17. Abbood, H.D.; Benigni, A. Data-Driven Modeling of a Commercial Photovoltaic Microinverter. *Model. Simul. Eng.* **2018**, *2018*, 5280681. [CrossRef]
18. Wang, P.; Chen, X.; Tong, C.; Jia, P.; Wen, C. Large-and small-signal average-value modeling of dual-active-bridge DC–DC converter with triple-phase-shift control. *IEEE Trans. Power Electron.* **2021**, *36*, 9237–9250. [CrossRef]

19. Yan, D.; Yang, C.; Hang, L.; He, Y.; Luo, P.; Shen, L.; Zeng, P. Review of general modeling approaches of power converters. *Chin. J. Electr. Eng.* **2021**, *7*, 27–36. [CrossRef]
20. Bai, H.; Liu, C.; Breaz, E.; Al-Haddad, K.; Gao, F. A review on the device-level real-time simulation of power electronic converters: Motivations for improving performance. *IEEE Ind. Electron. Mag.* **2020**, *15*, 12–27. [CrossRef]
21. Maksimovic, D.; Stankovic, A.M.; Thottuvelil, V.J.; Verghese, G.C. Modeling and simulation of power electronic converters. *Proc. IEEE* **2001**, *89*, 898–912. [CrossRef]
22. Kanimozhi, K.; Prabhakaran, K.; Harischandrappa, N.; Venkatesaperumal, B. Development of Small Signal Model and Stability Analysis of PV-Grid Integration System for EV Charging Application. *IEEE J. Emerg. Sel. Top. Ind. Electron.* **2023**, *5*, 274–284.
23. Ridley, R.B. A new, continuous-time model for current-mode control (power converters). *IEEE Trans. Power Electron.* **1991**, *6*, 271–280. [CrossRef]
24. Pavlovic, T.; Bjazic, T.; Ban, Z. Simplified averaged models of DC–DC power converters suitable for controller design and microgrid simulation. *IEEE Trans. Power Electron.* **2012**, *28*, 3266–3275. [CrossRef]
25. Amini Akbarabadi, S. Circuit Averaging and Numerical Average Value Modeling of Flyback Converter in CCM and DCM Including Parasitics and Snubbers. Ph.D. Thesis, University of British Columbia, Vancouver, BC, Canada, 2014. [CrossRef]
26. Sucu, M. Parametric Average Value Modeling of Flyback Converters in CCM and DCM Including Parasitics and Snubbers. Ph.D. Thesis, University of British Columbia, Vancouver, BC, Canada, 2011.
27. Feng, W.; Chen, Y.; Jiang, J.; Jiang, W. Modeling and controller design of flyback converter operating in DCM for LED constant current drive. In Proceedings of the IOP Conference Series: Earth and Environmental Science, Changsha, China, 18–20 September 2020; IOP Publishing: Bristol, UK, 2020; Volume 512, p. 012172.
28. Tahami, F.; Abedi, M.; Rezaei, K. Optimum nonlinear model predictive controller design for Flyback PFC rectifiers. In Proceedings of the 2010 IEEE Symposium on Industrial Electronics and Applications (ISIEA), Penang, Malaysia, 3–5 October 2010; IEEE: Piscataway, NJ, USA, 2010; pp. 70–75.
29. Akbarabadi, S.A.; Atighechi, H.; Jatskevich, J. Circuit-averaged and state-space-averaged-value modeling of second-order flyback converter in CCM and DCM including conduction losses. In Proceedings of the 4th International Conference on Power Engineering, Energy and Electrical Drives, Istanbul, Turkey, 13–17 May 2013; IEEE: Piscataway, NJ, USA, 2013; pp. 995–1000.
30. Gu, D.; Xi, J.; He, L. A digital PWM controller of MHz active clamp flyback with GaN devices for AC-DC adapter. In Proceedings of the IECON 2019—45th Annual Conference of the IEEE Industrial Electronics Society, Lisbon, Portugal, 14–17 October 2019; IEEE: Piscataway, NJ, USA, 2019; Volume 1, pp. 1496–1501.
31. Andreescu, G.D.; Cornea, O.; Muntean, N.; Guran, E. Bidirectional flyback inverter with low output voltage THD. In Proceedings of the 2015 IEEE 10th Jubilee International Symposium on Applied Computational Intelligence and Informatics, Timisoara, Romania, 21–23 May 2015; IEEE: Piscataway, NJ, USA, 2015; pp. 95–99.
32. Angulo, F.; Giraldo, D.E.; Rojas, S.; Bolaños, M.A.; Osorio, G.; Astaiza, N.; Mina-Casaran, J.D.; Herrera, W. A Novel Nonlinear Averaged Model for a Flyback Converter with Peak Current Mode Control. In Proceedings of the 2024 International Conference on Electrical, Computer and Energy Technologies (ICECET), Sydney, Australia, 25–27 July 2024; pp. 1–6. [CrossRef]
33. Hart, D.W.; Hart, D.W. *Power Electronics*; McGraw-Hill: New York, NY, USA, 2011; Volume 166.
34. Rashid, M.H. *Power Electronics Handbook*, 5th ed.; Butterworth-Heinemann: Oxford, UK, 2024.

Disclaimer/Publisher's Note: The statements, opinions and data contained in all publications are solely those of the individual author(s) and contributor(s) and not of MDPI and/or the editor(s). MDPI and/or the editor(s) disclaim responsibility for any injury to people or property resulting from any ideas, methods, instructions or products referred to in the content.